

Structural characterization and low-temperature properties of Ru/C multilayer monochromators with different periodic thicknesses

Hui Jiang,* Yan He, Yumei He, Aiguo Li, Hua Wang, Yi Zheng and Zhaohui Dong

Received 2 July 2015
Accepted 23 September 2015

Edited by G. E. Ice, Oak Ridge National Laboratory, USA

Keywords: multilayer; cryogenic cooling; interdiffusion; interfacial roughness; stress.

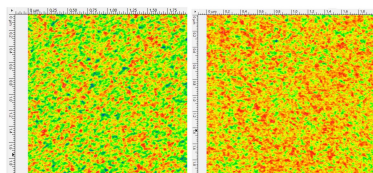
Shanghai Synchrotron Radiation Facility, Shanghai Institute of Applied Physics, Chinese Academy of Sciences, Zhangheng Road 239, Pudong District, Shanghai 201204, People's Republic of China.

*Correspondence e-mail: jianghui@sinap.ac.cn

Ru/C multilayer monochromators with different periodic thicknesses were investigated using X-ray grazing-incidence reflectivity, diffuse scattering, Bragg imaging, morphology testing, *etc.* before and after cryogenic cooling. Quantitative analyses enabled the determination of the key multilayer structural parameters for samples with different periodic thicknesses, especially the influence from the ruthenium crystallization. The results also reveal that the basic structures and reflection performance keep stable after cryogenic cooling. The low-temperature treatment smoothed the surfaces and interfaces and changed the growth characteristic to a low-frequency surface figure. This study helps with the understanding of the structure evolution of multilayer monochromators during cryogenic cooling and presents sufficient experimental proof for using cryogenically cooled multilayer monochromators in a high-thermal-load undulator beamline.

1. Introduction

One of the main applications for X-ray multilayer mirrors is at synchrotron radiation or free-electron laser facilities. Energy selecting [monochromator (Hexemer *et al.*, 2010), supermirror (Erko *et al.*, 1995)], amplitude or direction selecting [reflector, beam splitter (Haga *et al.*, 1998), focusing component (Kang *et al.*, 2008; Mimura *et al.*, 2010)] and phase selecting [polarizer (Wang *et al.*, 2006) and chirped mirror (Schultze *et al.*, 2007)] are three important uses. In the hard X-ray region, a double-crystal monochromator (DCM) has been widely used owing to its excellent energy resolution of beyond 0.1%. But some experiments pay more attention to high flux rather than high-energy resolution such as X-ray fluorescence and full-field imaging. To date, microprobe and nanoprobe beamlines have been rapidly developed. In order to compensate the flux loss during the process of focusing, it is meaningful to increase the incident flux before the focusing component. A double multilayer monochromator (DMM) can increase the integrated intensity by about a factor of ten with broadened bandwidth. A DCM and a DMM are always equipped for alternate operation in so-called high-resolution mode and high-throughput mode, respectively, and are present in many beamlines such as the BM5 and ID19 beamlines at the ESRF, the 2-BM and 32-ID beamlines at the APS, the TOMCAT beamline at the SLS and the BAM beamline at the BESSY-II. Owing to a relatively low flux for the bending-magnet or wiggler beamlines, water-cooling systems can serve well on these DMMs. When the power density of thermal load at the



first mirror is much larger than 1 W mm^{-2} on an undulator beamline, a cryogenic cooling system is necessary to prevent the mirror from serious thermal deformation and even stress-driven film delamination. At present, only a few DMMs are being used on the undulator beamline at PETRA-III (Schroer *et al.*, 2010). Lack of valid experimental data and experience restricts beamline scientists to estimate the influences on multilayer interfacial structure, internal stress and surface figure from the process of cryogenic cooling. It is also difficult to use a common heat conduction model or finite-element analysis to estimate these influences owing to the size and boundary effects of nanometre films (Cheaito *et al.*, 2012). It is worth considering the stability of the multilayer mirror when its temperature decreases to $\sim 80 \text{ K}$ from room temperature or its temperature returns to the room temperature rapidly from low temperature.

The Ru/C (Stampanoni *et al.*, 2006) or Ru/B₄C (Cloetens *et al.*, 2002) pair is an ideal structure for a monochromator at the photon energy range 10–20 keV. In this paper, several Ru/C multilayer monochromators with different periodic thicknesses were characterized by hard X-ray grazing-incidence reflectivity, diffuse scattering, X-ray Bragg imaging, laser interferometer and atomic force microscopy (AFM) techniques before and after cryogenic cooling with liquid nitrogen (LN₂) and compared systemically.

2. Experiments and methods

2.1. Sample

Six multilayer samples were deposited by DC magnetron sputtering on silicon substrates with a size of $35 \text{ mm} \times 22.5 \text{ mm}$ and a thickness of 0.75 mm at room temperature by Incoatec GmbH, Germany. The target periodic thicknesses for these samples are 3, 4 and 5 nm. The thickness ratios and the period numbers for all samples are 0.5 and 100, respectively.

2.2. Experiment

All samples were measured by hard X-ray grazing-incidence reflectivity (XRR), diffuse scattering (XDS) and high-angle reflectivity at the X-ray diffraction beamline (BL14B1), and by X-ray Bragg imaging at the hard X-ray micro-focusing beamline (BL15U1) of the Shanghai Synchrotron Radiation Facility (SSRF) before and after cryogenic cooling.

The SSRF was operated at a current of 240 mA at 3.5 GeV. The energy was 10 keV during all measurements. BL14B1 is a bending-magnet beamline. The energy resolution was $\sim 1.5 \times 10^{-4}$ and the beam size at the sample was $\sim 0.4 \text{ mm} \times 0.4 \text{ mm}$. The reflectivity measurements operated with a θ - 2θ scan. The diffuse scattering measurement operated using a rocking-curve scan by fixing the detector (BEDE) and scanning incidence angle.

The insert device of BL15U1 is an undulator with a magnetic gap of 8.79 mm for an energy of 10 keV during the experiments. The secondary source slit separation was $250 \mu\text{m} \times 400 \mu\text{m}$. The sample stage was $\sim 6.01 \text{ m}$ downstream of the secondary source slit. The multilayer was rotated around the

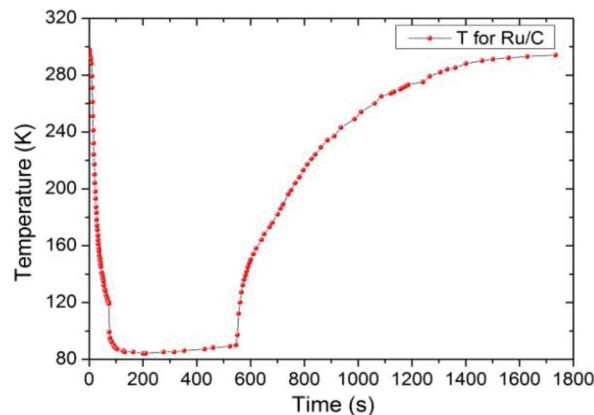


Figure 1 Temperature of the multilayer as a function of time during the experiment.

axis normal direction to the ground. The rotation angle was operated at the grazing-incidence region. The imaging detection system, which was placed 6.155 m behind the secondary source slit, was a LuAG:Ce screen coupled with a microscope objective lens (Navitar) to a digital CCD camera (Prosilica Inc.). The gain was 2 and the exposure time was 0.1 s. The sensor size was 1360×1024 pixels with a pixel size of $\sim 0.9 \mu\text{m}$.

After the first measurements, all samples were soaked in LN₂ and then taken out of the container until the LN₂ had evaporated and the temperature of the samples had returned to room temperature. The temperature was recorded using a platinum resistance thermometer (TXY509). The change in the temperature is shown in Fig. 1.

The stress of all multilayers was measured using a Zygo GPI XP/D Fizeau interferometer by detecting the substrate curvature. The surface roughness of all multilayers was measured using a Veeco di Nanoscope atomic force microscope.

2.3. X-ray reflectivity and diffuse scattering

The reflection from a periodic multilayer obeys the modified Bragg law by taking into account small deviations of the refraction indices of layer materials. According to the positions of different Bragg reflection maxima, based on the method of least squares, the periodic thickness can be calculated. The theoretical hard X-ray reflectivity curve as a function of grazing-incidence angle can be calculated based on Parratt's recurrence formula (Parratt, 1954). Because the sample size was smaller than the beam footprint near the critical angle, the intensity of the reflectivity curve was corrected.

Interfacial roughness and interdiffusion deteriorate the reflectivity curve in a similar way. X-ray diffuse scattering is a direct technique for determining interfacial roughness. A distorted-wave Born approximation (DWBA) model (Holy, 1994) is suitable for the situation of slightly rough interfaces. The whole diffuse scattering signal (Stoef & Sakurai, 1997) is represented by

$$I_{\text{diff}} = I_0 \varphi \sum_{j,k=1}^N |n_j^2 - n_{j+1}^2|^2 \sum_{m,n=0}^3 S_{j,k}^{mn}(q_x) \tilde{G}_j^m(\tilde{G}_k^n) \times \exp\left(-\frac{1}{2}\left\{(q_{z,j}^m \sigma_j)^2 + [(q_{z,k}^n) \sigma_k]^2\right\}\right), \quad (1)$$

where I_0 is the incident flux, φ is the instrument parameter, n_j and σ_j are the complex refractive index and interfacial roughness of the j th layer, respectively, q_x and q_z are the wavevectors along and perpendicular to the sample surface in reciprocal space, respectively, G_j^m are the four mutual products of the transmitted and reflected waves [T_i (or R_i) and T_s (or R_s)], and $S(q_x)$ is the structure factor

$$S_{j,k} = \int_0^\infty C_{j,k}(x) \cos(q_x x) dx \exp\left(-|Z_j - Z_k|/\xi_\perp\right), \quad (2)$$

where ξ_\perp is the vertical correlation length (Pape *et al.*, 1998) and $C(x)$ is the lateral correlation function which is based on the self-affine characteristic of a rough interface (Sinha *et al.*, 1988),

$$C_{j,k}(x) = \frac{1}{2}[C_j(x) + C_k(x)], \quad (3)$$

$$C_j(x) = \sigma_j^2 \exp\left[-(x/\xi_\parallel)^{2h}\right],$$

where ξ_\parallel is the lateral correlation length and h is the fractal exponent.

Particle swarm optimization (Poli *et al.*, 2007) is an effective tool for global optimization and was used to search for the optimum structure parameters in a given constraint to realise a good agreement between the experimental and theoretical curves. Layer thickness, density and interfacial width can be obtained by fitting a grazing-incidence reflectivity curve. Further rocking-curve fitting that uses results from reflectivity-curve fitting as known parameters can obtain more detailed information including interfacial roughness, interdiffusion, fractal exponent, lateral and vertical correlation lengths. The time complexity for rocking-curve fitting was at least 32*N* times of that for reflectivity-curve fitting, where N is the period number for a multilayer. After a preliminary attempt, the vertical correlation length was large enough so that its value was fixed to be the total layer thickness, which decreases the computational complexity. All optimization algorithms were programmed using Fortran code.

2.4. Stress measurement

Laser interferometry was used to measure the deformation of the silicon substrate. The stress of the multilayers can be estimated by the well known Stoney equation (Stoney, 1909)

$$\sigma_f = \frac{E}{6(1-\nu)} \frac{d_s^2}{d_f} \frac{1}{R},$$

where E is Young's module (82 Gpa) and ν is the Poisson ratio (0.2) of the silicon substrate, d_s is the thickness of the substrate, d_f is the thickness of the multilayer structure and R is the radius of the substrate curvature.

3. Results and discussions

Six multilayers were measured using the X-ray grazing-incidence reflectivity technique before and after cryogenic cooling. As can be seen in Fig. 2 and Table 1, by using the modified Bragg equation calculation the periodic thicknesses were calculated accurately. Each layer thickness, layer density and interfacial width was obtained by the curve-fitting method based on a reasonable initial structure. There were discrepancies between the measured and fitting curves above $2\theta \simeq 7^\circ$ because the intensities of the measured data became so low that they could not be distinguished from the noise.

The interfacial widths for the Ru-on-C and C-on-Ru interfaces were ~ 0.31 nm and ~ 0.36 nm, respectively, before cryogenic cooling and then decreased to ~ 0.29 and ~ 0.31 nm. There was no apparent link between interfacial width and periodic thickness. The density of the ruthenium layers was close to that of bulk ruthenium.

The diffuse scattering technique afforded more structure information about the Ru/C multilayers. In order to improve the precision of the analysis, rocking-curve scans near different Bragg maxima were simultaneously fitted, as can be seen in Fig. 3 and Table 2. The interfacial width obtained by XRR can be separated into two parts, *i.e.* interfacial roughness and interdiffusion, by fitting the curves of the rocking-curve

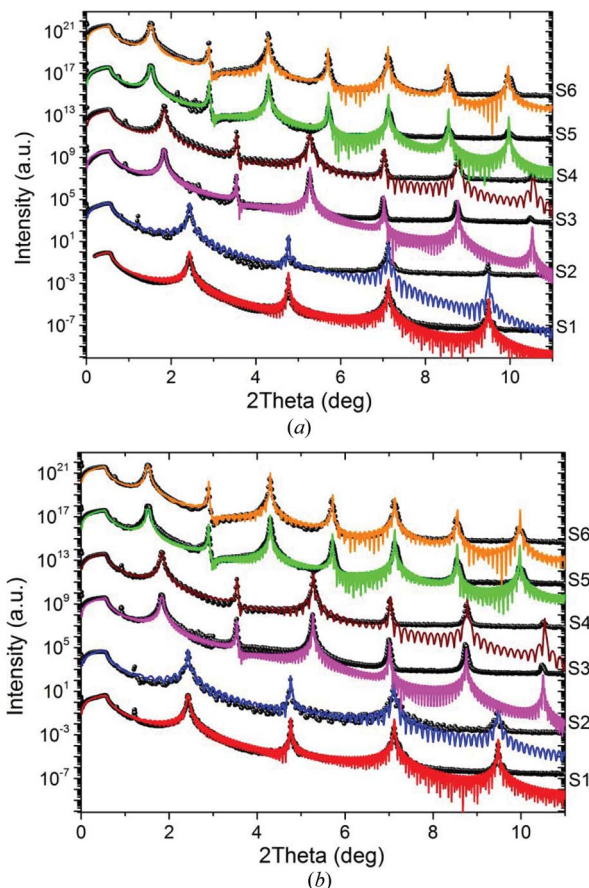


Figure 2 X-ray grazing-incidence reflectivity (black filled circles) and fitted (colored curves) curves for the Ru/C multilayers before (a) and after (b) cryogenic cooling.

Table 1
Fitted structural parameters for the Ru/C multilayers before and after cryogenic cooling.

	Cryogenic cooling	Periodic thickness (nm)	Material	Thickness (nm)	Interfacial width (nm)	Density (% bulk)
S1	Before	3.01 ± 0.01	Ru	1.46 ± 0.02	0.39 ± 0.05	99.81 ± 1.12
	After	3.01 ± 0.01	Ru	1.46 ± 0.01	0.34 ± 0.03	99.78 ± 3.08
S2	Before	3.01 ± 0.01	Ru	1.45 ± 0.02	0.39 ± 0.05	99.89 ± 3.10
	After	3.01 ± 0.01	Ru	1.46 ± 0.03	0.35 ± 0.02	91.41 ± 6.11
S3	Before	4.08 ± 0.01	Ru	2.06 ± 0.04	0.39 ± 0.04	97.99 ± 3.16
	After	4.08 ± 0.01	Ru	2.06 ± 0.02	0.39 ± 0.04	99.97 ± 3.10
S4	Before	4.07 ± 0.01	Ru	2.07 ± 0.02	0.33 ± 0.03	97.69 ± 2.08
	After	4.08 ± 0.01	Ru	2.07 ± 0.03	0.31 ± 0.04	99.91 ± 4.01
S5	Before	5.02 ± 0.01	Ru	2.59 ± 0.03	0.37 ± 0.05	88.44 ± 6.15
	After	5.01 ± 0.01	Ru	2.58 ± 0.03	0.32 ± 0.04	99.98 ± 1.76
S6	Before	5.02 ± 0.01	Ru	2.60 ± 0.03	0.29 ± 0.04	99.79 ± 1.33
	After	5.02 ± 0.01	Ru	2.60 ± 0.02	0.25 ± 0.03	96.47 ± 3.12
			C	1.55 ± 0.02	0.27 ± 0.04	99.07 ± 2.97
			C	1.55 ± 0.03	0.34 ± 0.04	90.75 ± 7.19
			C	1.99 ± 0.03	0.32 ± 0.04	117.99 ± 9.11
			C	1.99 ± 0.03	0.33 ± 0.05	95.13 ± 3.14
			C	2.42 ± 0.02	0.30 ± 0.03	94.78 ± 4.09
			C	2.42 ± 0.02	0.25 ± 0.02	92.41 ± 3.05
			C	2.40 ± 0.03	0.24 ± 0.04	87.96 ± 2.88

scans. The interdiffusions were similar at the Ru-on-C and C-on-Ru interfaces but the interfacial roughness at the C-on-Ru interface was larger. The low temperature smoothed the interfaces but had no clear influence on interdiffusion. The fractal exponents of the carbon layers were ~0.6 for all samples while the fractal exponents of the ruthenium layer increased with periodic thickness from ~0.45 to ~0.7. The lateral correlation length of the ruthenium layers increased from ~52.6 nm to ~85.2 nm while that of the carbon layers increased from ~7.7 nm to ~10.4 nm with periodic thickness. The lateral correlation length of the ruthenium layers was found to decrease while that of the carbon layers increased after cryogenic cooling. AFM (Fig. 4) was used to measure the surface roughness of S1, S3 and S5 at a scan range of 5 μm × 5 μm. Although AFM works at a different spatial frequency from X-ray techniques, it was found that cryogenic cooling slightly decreased the surface roughness as well.

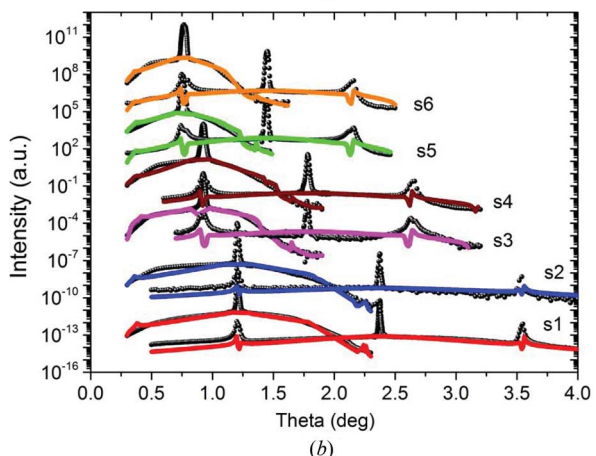
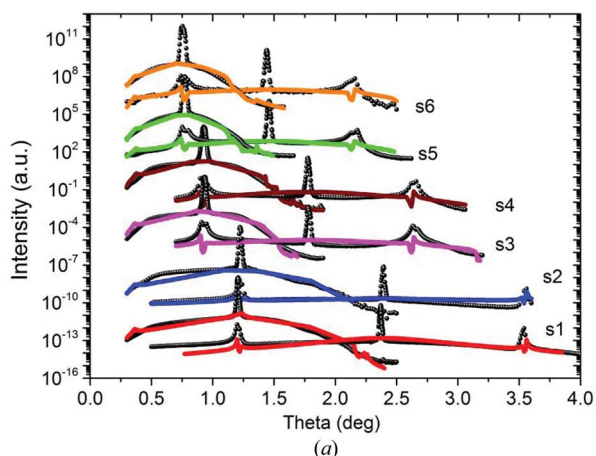


Figure 3
Rocking-curve scans near the first and the second Bragg maxima (black filled circles) and their fitted curves (colored curves) for the Ru/C multilayers before (a) and after (b) cryogenic cooling.

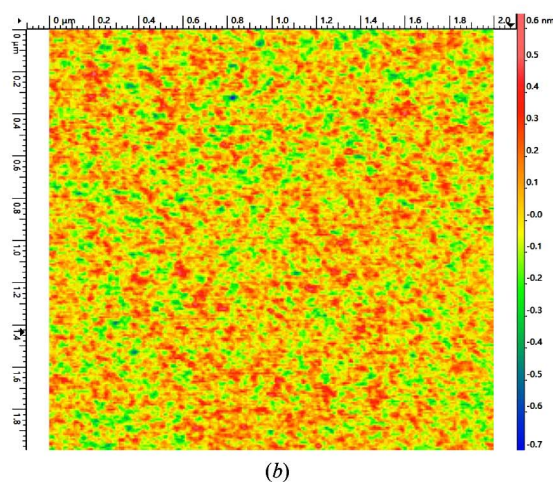
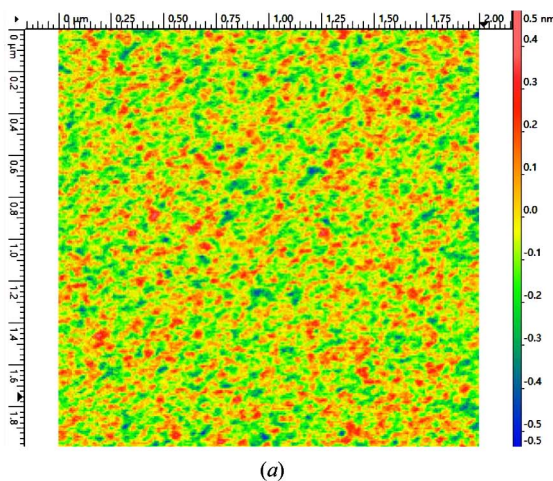


Figure 4
Surface roughness of S1 measured using AFM before (a) and after (b) cryogenic cooling.

Table 2

Characterization results of Ru/C multilayers using the X-ray diffuse scattering technique and AFM before and after cryogenic cooling.

	Cryogenic cooling	Material	Interfacial roughness (nm)	Interdiffusion (nm)	Fractal exponent	Lateral correlation length (nm)	Vertical correlation length (nm)	Surface roughness by AFM (nm)
S1	Before	Ru	0.35 ± 0.03	0.17 ± 0.08	0.43 ± 0.01	52.06 ± 16.11	300	0.17 ± 0.01
		C	0.24 ± 0.05	0.16 ± 0.08	0.66 ± 0.01	8.61 ± 2.07		
	After	Ru	0.31 ± 0.07	0.14 ± 0.10	0.36 ± 0.01	43.92 ± 11.82	300	0.15 ± 0.02
		C	0.22 ± 0.03	0.16 ± 0.07	0.70 ± 0.01	9.54 ± 2.16		
S2	Before	Ru	0.35 ± 0.06	0.17 ± 0.11	0.47 ± 0.01	53.12 ± 13.94	300	–
		C	0.27 ± 0.03	0.21 ± 0.07	0.55 ± 0.02	6.80 ± 3.17		
	After	Ru	0.29 ± 0.05	0.20 ± 0.07	0.46 ± 0.02	47.10 ± 9.92	300	–
		C	0.24 ± 0.04	0.24 ± 0.07	0.58 ± 0.01	8.49 ± 2.78		
S3	Before	Ru	0.31 ± 0.03	0.24 ± 0.07	0.50 ± 0.01	78.33 ± 11.7	400	0.14 ± 0.02
		C	0.27 ± 0.03	0.24 ± 0.06	0.73 ± 0.02	7.92 ± 2.11		
	After	Ru	0.33 ± 0.04	0.21 ± 0.08	0.50 ± 0.02	71.35 ± 13.26	400	0.13 ± 0.01
		C	0.24 ± 0.03	0.21 ± 0.07	0.62 ± 0.01	10.01 ± 3.04		
S4	Before	Ru	0.27 ± 0.05	0.19 ± 0.08	0.58 ± 0.01	74.51 ± 9.04	400	–
		C	0.22 ± 0.04	0.24 ± 0.09	0.64 ± 0.01	9.59 ± 4.86		
	After	Ru	0.25 ± 0.04	0.18 ± 0.08	0.50 ± 0.01	82.00 ± 10.54	400	–
		C	0.21 ± 0.04	0.25 ± 0.07	0.64 ± 0.02	10.57 ± 2.35		
S5	Before	Ru	0.33 ± 0.03	0.17 ± 0.08	0.63 ± 0.01	87.39 ± 14.09	500	0.16 ± 0.02
		C	0.19 ± 0.02	0.23 ± 0.05	0.55 ± 0.02	11.11 ± 2.41		
	After	Ru	0.28 ± 0.03	0.15 ± 0.07	0.64 ± 0.01	86.83 ± 11.72	500	0.15 ± 0.01
		C	0.18 ± 0.02	0.17 ± 0.04	0.59 ± 0.01	12.24 ± 3.64		
S6	Before	Ru	0.21 ± 0.02	0.2 ± 0.06	0.79 ± 0.02	82.91 ± 10.05	500	–
		C	0.13 ± 0.02	0.2 ± 0.05	0.67 ± 0.02	9.61 ± 3.33		
	After	Ru	0.17 ± 0.02	0.18 ± 0.05	0.72 ± 0.01	90.25 ± 12.96	500	–
		C	0.12 ± 0.02	0.21 ± 0.06	0.66 ± 0.02	10.84 ± 1.97		

Fig. 5 reveals that there were Ru (101) crystalline phases in the multilayers. By increasing the thickness of the ruthenium layer, the amorphous ruthenium layer gradually transformed into a crystalline state. Based on the Scherrer equation (Patterson, 1939), the size of the Ru (101) crystals in the layer can be estimated. For samples S1, S3 and S5 the particle sizes were 1.27, 1.48 and 1.62 nm, respectively. The size difference was related to the change of the fractal exponent and the lateral correlation length. Because of the long-range disorder for the amorphous carbon layers, the fractal exponent almost remained constant. After cryogenic cooling, the crystalline states did not change for all samples.

As can be seen in Table 3, stress measurements reveal that, when the periodic thickness was 3 nm, the internal stress was tensile stress and changed to compressive stress with

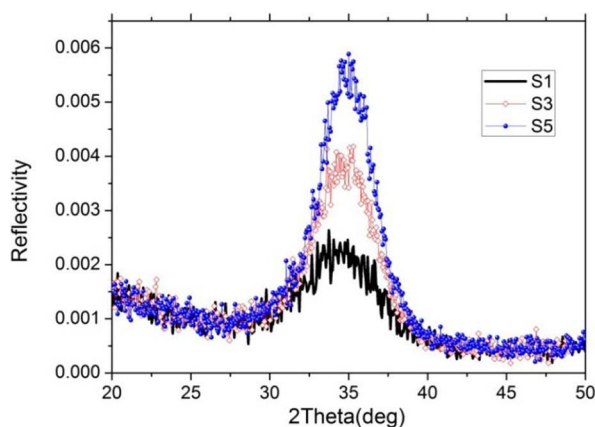


Figure 5

Ru (101) crystallographic planes measured by X-ray high-angle reflectivity for multilayers with different periodic thicknesses.

Table 3

Stress change for Ru/C multilayers before and after cryogenic cooling.

Sample	Stress before cryogenic cooling (MPa)	Stress after cryogenic cooling (MPa)
S1	382.24 ± 0.01	447.33 ± 0.02
S2	225.77 ± 0.01	245.42 ± 0.05
S3	–700.01 ± 0.08	–681.79 ± 0.07
S4	–1180.52 ± 0.10	–1007.60 ± 0.06
S5	–818.63 ± 0.08	–728.10 ± 0.07
S6	–1044.18 ± 0.04	–978.66 ± 0.07

increasing periodic thickness. This may be a result of the ruthenium crystalline state. After cryogenic cooling, the stress in the multilayer slightly increased. By combining the data extracted from XRR and XDS, it was found that the stress increase relates to the interface smoothing process. The structure did not recover totally with the temperature returning to room temperature. The contraction of the multilayer stack is more obvious than in the substrate after the whole process, resulting in increasing stress in the multilayer. This process did not generate any phase transition but decreased the spacing of the deposited island or columnar structure of the multilayer, leading to a smoothing of the interfaces.

Fig. 6 shows the first Bragg reflection imaging of samples S1, S3 and S5 before and after cryogenic cooling. The Bragg angles are 1.216°, 0.926° and 0.756°, respectively, with an accuracy of 0.002°. The brightness of the imaging is proportional to the reflectivity. The reflectivities before and after cryogenic cooling are almost unchanged. Clear interference stripes can be found especially along the tangential direction. The distribution of the interference stripes is related to the

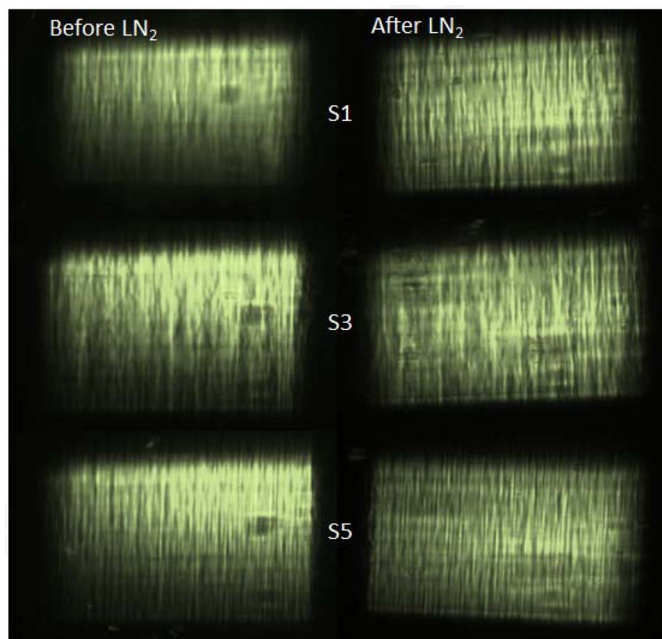


Figure 6
Reflection imaging of S1, S3 and S5 before and after cryogenic cooling.

phase errors resulting from the slope error of the mirror (Mimura *et al.*, 2004; Rommeveaux & Souvorov, 1999). The multi-resolution approach, one of the most important techniques in wavelet analysis, can be used to decompose the intensity profile into different levels including an approximate signal and several detailed signals with different spatial frequencies, localized in both the space and frequency regions.

At each level, the signal which is the approximated signal of the last level can be separated into a new approximated signal and a detailed signal with half of the spatial frequency range. Fig. 7 demonstrates the decomposition of the reflected intensity profiles before and after cryogenic cooling of S5 using a multi-resolution approach with five levels. Relating the intensity profiles on the screen to the multilayer surface, the detailed signals (Detail 1 and 2 in Fig. 7) with frequency of $357.3\text{--}1428.57\ \mu\text{m}^{-1}$ before and after cryogenic cooling were in good agreement. The detailed signals (Detail 3 and 4) with frequency of $89.4\text{--}357.3\ \mu\text{m}^{-1}$ before and after cryogenic cooling have similar amplitudes but weak correlation. The low-frequency signals (Detail 5 and Approximation) with frequency of $<89.4\ \mu\text{m}^{-1}$ after cryogenic cooling have decreased amplitudes and keep a strong correlation. The results reveal that the high-frequency signals contributed by the layer growth kept stable and the low-frequency signals from the surface figure decreased during the temperature change, which proves the analysis by X-ray scattering and stress measurement that the cryogenic cooling did not change the chemical characteristics of the multilayers but changed the figure error and stress. The decrease of the interfacial roughness was mainly reflected in the low-frequency region.

4. Conclusions

In order to study the low-temperature properties of key Ru/C multilayer monochromators for synchrotron radiation, X-ray grazing-incidence reflectivity, diffuse scattering, Bragg imaging and morphology testing were used to characterize the multilayer structure with different periodic thicknesses

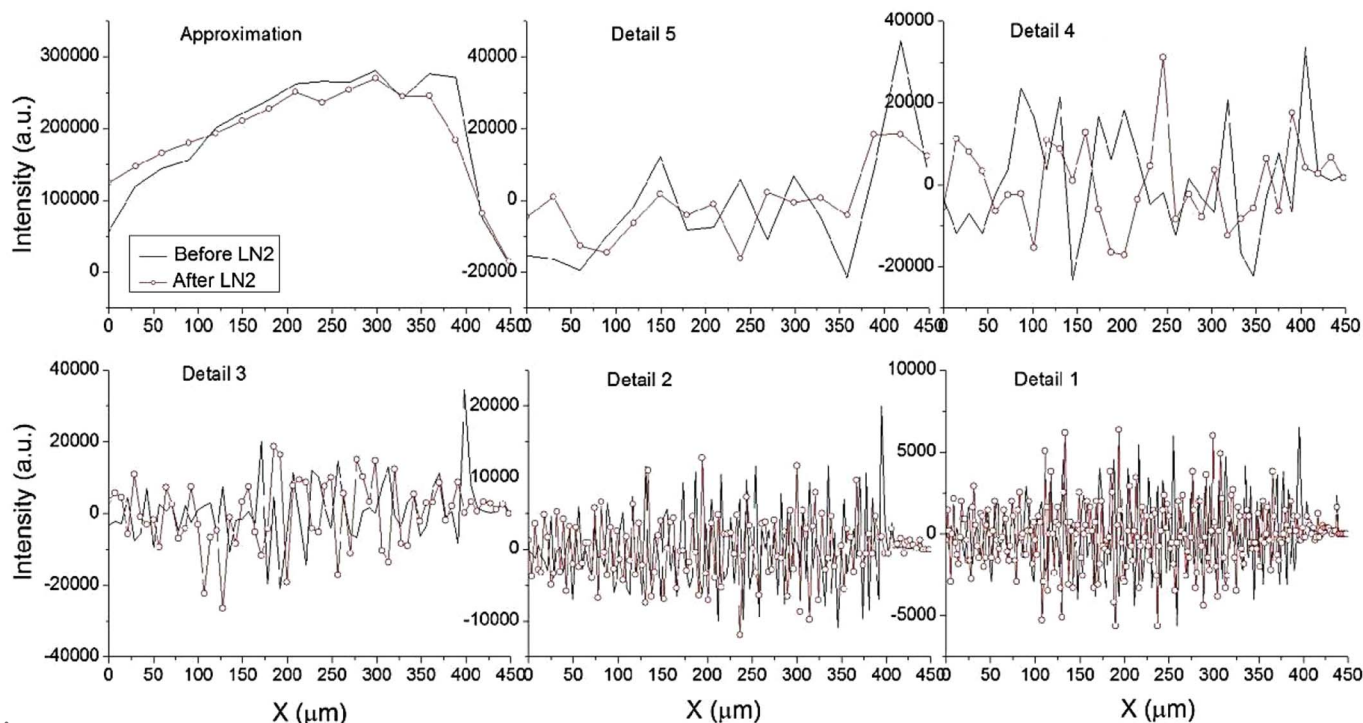


Figure 7
Multi-resolution wavelet decomposition for the beam spots of S5 before and after cryogenic cooling.

synthetically, including information of the layer thickness, density, interfacial roughness, interdiffusion, correlation length, internal stress, *etc.* After cryogenic cooling, the basic structure parameters kept stable and the interfaces tended to be smooth due to internal stress change. At-wavelength reflection performances were maintained as well. This study affords strong support for the use of Ru/C multilayer monochromators safely in the cryogenic cooling environment.

Acknowledgements

Incoatec GmbH is thanked for the fabrication of all multilayer monochromators. The authors would like to thank their colleagues from the SSRF: Drs Haozhi Lei and Yi Zhang for AFM measurement, Drs Yifei Zhang and Hongxin Luo for interferometer measurement, and Drs Li Li and Xingmin Zhang for helping in BL14B1 reflectivity and scattering measurements. This work was supported by the National Natural Science Foundation of China (grant No. 11304339), the Knowledge Innovation Program of Chinese Academy of Sciences and the Scientific Research Foundation for the Returned Overseas Chinese Scholars, State Education Ministry.

References

- Cheaito, R., Duda, J. C., Beechem, T. E., Hattar, K., Ihlefeld, J. F., Medlin, D. L., Rodriguez, M. A., Campion, M. J., Piekos, E. S. & Hopkins, P. E. (2012). *Phys. Rev. Lett.* **109**, 195901.
- Cloetens, P., Ludwig, W., Boller, E., Helfen, L., Salvo, L., Mache, R. & Schlenker, M. (2002). *Proc. SPIE*, **4503**, 82.
- Erko, A., Schäfers, F., Vidal, B., Yakshin, A., Pietsch, U. & Mahler, W. (1995). *Rev. Sci. Instrum.* **66**, 4845–4846.
- Haga, T., Tinone, M. C. K., Shimada, M., Ohkubo, T. & Ozawa, A. (1998). *J. Synchrotron Rad.* **5**, 690–692.
- Hexemer, A., Bras, W., Glossinger, J., Schaible, E., Gann, E., Kirian, R., MacDowell, A., Church, M., Rude, B. & Padmore, H. (2010). *J. Phys. Conf. Ser.* **247**, 012007.
- Holy, V. (1994). *Appl. Phys. A*, **58**, 173–180.
- Kang, H. C., Yan, H., Winarski, R. P., Holt, M. V., Maser, J., Liu, C., Conley, R., Vogt, S., Macrander, A. T. & Stephenson, G. B. (2008). *Appl. Phys. Lett.* **92**, 221114.
- Mimura, H., Handa, S., Kimura, T., Yumoto, H., Yamakawa, D., Yokoyama, H., Matsuyama, S., Inagaki, K., Yamamura, K., Sano, Y., Tamasaku, K., Nishino, Y., Yabashi, M., Ishikawa, T. & Yamauchi, K. (2010). *Nat. Phys.* **6**, 122–125.
- Mimura, H., Yamauchi, K., Yamamura, K., Kubota, A., Matsuyama, S., Sano, Y., Ueno, K., Endo, K., Nishino, Y., Tamasaku, K., Yabashi, M., Ishikawa, T. & Mori, Y. (2004). *J. Synchrotron Rad.* **11**, 343–346.
- Pape, I., Hase, T. P. A., Tanner, B. K. & Wormington, M. (1998). *Physica B*, **253**, 278–289.
- Parratt, L. G. (1954). *Phys. Rev.* **95**, 359–369.
- Patterson, A. (1939). *Phys. Rev.* **56**, 978–982.
- Poli, R., Kennedy, J. & Blackwell, T. (2007). *Swarm Intell.* **1**, 33–57.
- Rommeveaux, A. & Souvorov, A. (1999). *Proc. SPIE*, **3773**, 70.
- Schroer, C. G., Boye, P., Feldkamp, J. M., Patommel, J., Samberg, D., Schropp, A., Schwab, A., Stephan, S., Falkenberg, G., Wellenreuther, G. & Reimers, N. (2010). *Nucl. Instrum. Methods Phys. Res. A*, **616**, 93–97.
- Schultze, M., Goulielmakis, E., Uiberacker, M., Hofstetter, M., Kim, J., Kim, D., Krausz, F. & Kleineberg, U. (2007). *New J. Phys.* **9**, 243.
- Sinha, S., Sirota, E. B., Garoff, S. & Stanley, H. B. (1988). *Phys. Rev. B*, **38**, 2297–2311.
- Stampanoni, M., Groso, A., Isenegger, A., Mikuljan, G., Chen, Q., Bertrand, A., Henein, S., Betemps, R., Frommherz, U., Böhrer, P., Meister, D., Lange, M. & Abela, R. (2006). *Proc. SPIE*, **6318**, 63180M.
- Stoev, K. & Sakurai, K. (1997). *Rigaku J.* **14**, 22–37.
- Stoney, G. G. (1909). *Proc. R. Soc. A*, **82**, 172–175.
- Wang, Z., Wang, H., Zhu, J., Wang, F., Gu, Z., Chen, L., Michette, A. G., Powell, A. K., Pfauntsch, S. J. & Schäfers, F. (2006). *J. Appl. Phys.* **99**, 056108.